Measurement of Phase and Amplitude Error Distributions in Arrayed-Waveguide Grating Multi/Demultiplexers Based on Dispersive Waveguide

Hiroaki Yamada, *Member, IEEE*, Hiroaki Sanjoh, Masaki Kohtoku, Kazumasa Takada, *Member, IEEE*, and Katsunari Okamoto, *Senior Member, IEEE, Member OSA*

***Abstract*—We measured the phase and amplitude error distributions in InP-based arrayed-waveguide grating (AWG) multi/demultiplexers using Fourier transform spectroscopy with interferogram restoration. The interferogram restoration was used to reduce the effect of the group-velocity dispersion of the waveguide. It was based on a wavenumber scale transformation or a dispersion balance between two arms in the interferometer. We derived a criterion for choosing the appropriate restoration method by estimating the worst-case measurement error in the presence of second order dispersion. After selecting a method using the derived criterion, we obtained isolated fringe patterns, from which we were able to obtain the phase and amplitude distributions in 50 and 200 GHz AWGs. Using the obtained distributions, we examined the origin of the crosstalk and chromatic dispersion in InP-based AWGs. The results revealed that the main origin is phase error as found with SiO_2-based AWGs.**

***Index Terms*—Crosstalk, optical filters, waveguide grating, wavelength division multiplexing (WDM).**

I. Introduction

THE ARRAYED-WAVEGUIDE grating (AWG) multi/demultiplexer [1]–[5] is a key component in wavelength division multiplexing (WDM). The AWG is a multipath interferometer whose paths are constructed by using arrayed waveguides with a constant length difference between neighboring waveguides. The optical performance of this filter can be fully characterized by the phase and amplitude of each path. Thus, the knowledge of phase and amplitude distributions helps us to understand what should be improved to obtain high levels of performance, such as low crosstalk [6]–[8] and low dispersion. We have developed a method to measure the phase and amplitude of each path [9], [10]. This was based on Fourier transform spectroscopy with a low coherence interferometer. Using a broadband light source whose coherent length is shorter than the optical path length difference in the AWG, we obtain a series of isolated fringes, from each of which we derive the phase and amplitude for the corresponding path. We have reported some results relating to the measurement of SiO_2-based AWGs, including an improvement in the crosstalk by phase error compensation [6]–[8] and the origin of the crosstalk degradation [11] and chromatic dispersion [12].

AWGs based on other materials, such as InP [13]–[15], polymer [16] and $LiNbO_3$ [17], have already been reported. Of these, InP-based AWGs show a superior potential for monolithic integration with active components such as detectors, lasers, amplifiers, modulators and switches [18]–[22]. It is also important to measure the phase and amplitude distributions of AWGs based on this material in order to obtain information allowing us to improve their performance. One problem that arises when measuring the distribution of an AWG based on dispersive material is the fringe broadening caused by the group-velocity dispersion (GVD). This fringe broadening leads to a degradation in measurement accuracy, because the overlap of neighboring fringes becomes serious. Thus, the effect of dispersion makes it difficult to estimate accurately the phase and amplitude distributions of AWGs with a large dispersion and a small path difference.

The aim of this paper is to show how to measure accurately the phase and amplitude errors of an AWG based on a dispersive waveguide. Section II derives the measurement error in phase and amplitude in the presence of second order GVD. Then we estimate the measurable limit for the AWG and the dispersion parameters. Section III considers two methods for reducing the measurement error caused by the GVD. One method is to balance the dispersion in the test arm with an equal dispersion in the reference arm. However, this balance method can only eliminate the dispersion at a particular path in the AWG and the dispersion effect still exists at other paths. Another method is a numerical approach based on a wavenumber scale transformation [23], [24]. Although this method requires information on dispersion parameters, the dispersion effect can be eliminated at any path in the AWG. In Section III, we clarify the criterion for a suitable choice of restoration method by estimating the worst-case measurement error. Using this criterion, we successfully measure the phase and amplitude distributions in 50 and 200 GHz InP-based AWGs. Section IV presents these experimental results. Section V discusses the effect of the phase and amplitude error distributions on the crosstalk and the chromatic dispersion in the InP-based AWG.

Manuscript received March 16, 2000.

H. Yamada, K. Takada, and K. Okamoto are with NTT Photonics Laboratories, Ibaraki, Japan (e-mail: hyamada@iba.iecl.ntt.co.jp).

H. Sanjoh and M. Kohtoku are with NTT Photonics Laboratories, Kanagawa 243–0198, Japan.

Publisher Item Identifier S 0733-8724(00)08082-8.

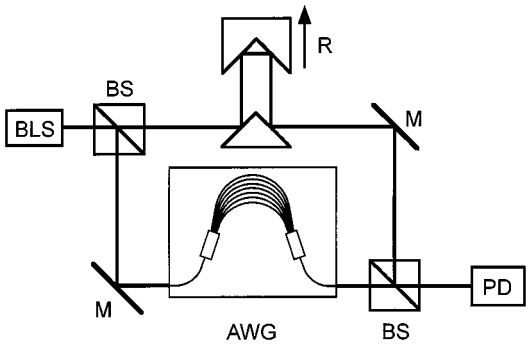

Fig. 1. Schematic setup for phase and amplitude distribution measurement (BLS: broad-band light source; BS: beam splitter; R: retroreflector; M: mirror; and PD: photodiode)

II. Measurement Error in Phase and Amplitude Distributions in the Presence of Second-Order Dispersion

A. Measurement Principle

The measurement of the phase and amplitude distributions of the AWG is based on Fourier transform spectroscopy with a low coherence interferometer [9], [10]. Fig. 1 shows a schematic of the setup for the distribution measurement. The setup consists of a Mach–Zehnder interferometer (MZI) with a broad-band light source. The AWG under test is placed in one arm of the interferometer. Since the AWG contains M paths with a constant length difference ΔL between neighboring waveguides, the transfer function can be written as

$$H(\sigma) = \sum_{p=0}^{M-1} a_p \exp(-j\phi_p) \exp[-j\beta(\sigma)L_p] \tag{1}$$

where a_p and ϕ_p are the amplitude and phase of the light propagating through the pth arrayed waveguide, $\beta(\sigma)$ is the propagation constant of the waveguide, $L_p = L+[p-(M-1)/2]\Delta L$ is the length of the pth path and L is the length of the central path which contains the input and output waveguides and two slab waveguides. By changing the path length x of the other arm of the interferometer, we obtain the interferogram

$$I(x) = \int_{-\infty}^{\infty} G(\sigma)H(\sigma)\exp(j2\pi x\sigma)\,d\sigma = \sum_{p=0}^{M-1} I_p(x) \tag{2}$$

where $G(\sigma)$ is the power spectrum of the light source; $I_p(x)$ is related to the fringe for the pth path in the AWG and is given by

$$I_p(x) = \int_{-\infty}^{\infty} a_p e^{-j\phi_p} G(\sigma)\exp[j2\pi x\sigma - j\beta(\sigma)L_p]\,d\sigma \tag{3}$$

The value of $G(\sigma)H(\sigma)$ for $\sigma < 0$ is defined by its complex conjugation: $G(-\sigma)H(-\sigma) = G^*(\sigma)H^*(\sigma)$. If we can extract the fringe $I_p(x)$ from the interferogram $I(x)$, we can calculate a_p and ϕ_p from the Fourier transform of $I_p(x)$

$$S_p(\sigma)G(\sigma) = \int_{-\infty}^{\infty} I_p(x)\exp(-j2\pi x\sigma)\,dx \tag{4}$$

$$S_p(\sigma) = a_p \exp\{-j[\beta(\sigma)L_p + \phi_p]\} \tag{5}$$

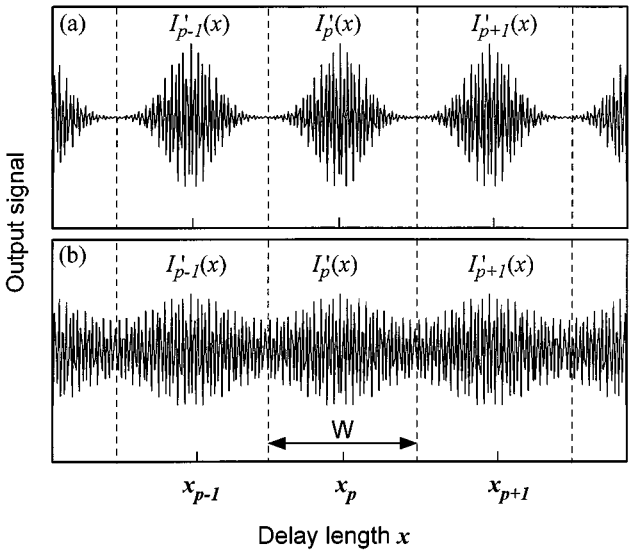

Fig. 2. Schematic of a part of an interferogram for the AWG, when the fringe overlap is (a) small and (b) large because of the GVD in the waveguide

where $S_p(\sigma)$ is the transfer function of the pth path.

B. Derivation of Measurement Error for a Dispersive Waveguide

In a practical measurement, we cannot obtain a completely separated fringe $I_p(x)$, because there are also contributions from neighboring fringes, $I_{p\pm k}(x)(k = 1, 2, 3\ldots)$ near the fringe peak position x_p, as shown in Fig. 2. As the figure shows, the contributions from the neighboring fringes increase with increasing GVD. The truncation of $I(x)$ is an effective way of minimizing these contributions. If we use W as the truncation width, then the truncated fringe $I'_p(x)$ can be expressed as

$$I'_p(x) = I(x)\Pi[(x - x_p)/W] \tag{6}$$

where $\Pi(x)$ is a truncation function defined by

$$\Pi(x) = \begin{cases} 1 & \text{for } |x| \le 1/2 \\ 0 & \text{otherwise} \end{cases} \tag{7}$$

Because of the truncation and fringe overlap, $I'_p(x)$ is not equal to $I_p(x)$ and this causes measurement errors in a_p and ϕ_p. We have derived the measurement error for a nondispersive waveguide [10]. Here, we will derive the measurement error for a dispersive waveguide by extending that for a nondispersive waveguide.

The fringe $I_p(x)$ for a dispersive waveguide can be expressed analytically when $\beta(\sigma)$ and $G(\sigma)$, respectively, are given by

$$\begin{aligned}\beta(\sigma) &= \beta_0 + \beta_1(\sigma - \sigma_0) + \frac{\beta_2}{2}(\sigma - \sigma_0)^2 \\ &= 2\pi[n_{ph}\sigma_0 + n_{gr}(\sigma - \sigma_0)] + \frac{\beta_2}{2}(\sigma - \sigma_0)^2\end{aligned} \tag{8}$$

$$G(\sigma) = \exp\left[-\left(\frac{\sigma - \sigma_0}{\delta\sigma}\right)^2\right] \tag{9}$$

where

n_{ph} and n_{gr} phase and group indexes at σ_0, respectively;

$\delta\sigma$ half $1/e$ width;
σ_0 center wavelength of a light source.

Using (3), (8), and (9) and carrying out the integration, we obtain

$$I_p(x) = \frac{2}{\sqrt{\pi}\delta x}\, a_p \exp(-j\phi_p)(1+\varepsilon_p^2)^{-(1/4)} \times \exp\left[-\frac{(x-n_{gr}L_p)^2}{(1+\varepsilon_p^2)\delta x^2}\right] \times \cos[2\pi\sigma_0(x-n_{gr}L_p)+\rho(x)] \quad (10)$$

where

$$\rho(x) = \frac{\varepsilon_p}{1+\varepsilon_p^2}\left(\frac{x-n_{gr}L_p}{\delta x}\right)^2 - \frac{1}{2}\tan^{-1}(\varepsilon_p) \quad (11)$$

$$\varepsilon_p = \frac{\beta_2 L_p}{2\pi^2\delta x^2} \quad (12)$$

$\delta x = 1/(\pi\delta\sigma)$ is the half $1/e$-width for a nondispersive waveguide and ε_p is the dispersion factor. The envelope of $I_p(x)$ is broadened and its amplitude is depressed in the presence of β_2.

Using (6)–(7) and (10)–(12) and performing a Fourier transform of $I'_p(x)$, we obtain the transfer function

$$S'_p(\sigma) = \sum_{q=0,\pm1\ldots} a_{p-q}\exp\{-j[\beta(\sigma)L_{p-q}+\phi_{p-q}]\}U_{p,q} \quad (13)$$

where

$$U_{p,q} = \tfrac{1}{2}[\mathrm{erf}(D^+_{p,q}) - \mathrm{erf}(D^-_{p.q})] \quad (14)$$

$$D^{\pm}_{p,q} = \frac{\chi}{(1+j\varepsilon_{p,q})^{(1/2)}}\left(q\pm\frac{1}{2}\right) + j\alpha(1+j\varepsilon_{p,q})^{(1/2)} \quad (15)$$

$$\varepsilon_{p,q} = \frac{\beta_2(L_p - q\Delta L)}{2\pi^2\delta x^2} \quad (16)$$

$$\chi = n_{gr}\Delta L/\delta x \quad (17)$$

$$\alpha = (\sigma-\sigma_0)\pi\delta x \quad (18)$$

and erf() is the complex error function with a complex variable z, defined by

$$\mathrm{erf}(z) = \frac{2}{\sqrt{\pi}}\int_0^z e^{-u^2}\, du \quad (19)$$

In the derivation of the above equations, we used approximations $x_p \simeq n_{gr}L_p$, $x_{p-q} \simeq n_{gr}L_{p-q}$ and $W \simeq n_{gr}\Delta L$. Now, we can express the measurement error in phase θ and amplitude ξ as

$$\theta = -\arg[S'_p(\sigma)/S_p(\sigma)] \quad (20)$$

$$\xi = |S'_p(\sigma)/S_p(\sigma)| - 1 \quad (21)$$

where $S_p(\sigma)$ is the transfer function, as in (5), without any measurement error.

To conclude this section, we consider the effect of truncation with the help of the term for $q = 0$ in (13). We thus assume that the other terms, which correspond to the effect of the fringe overlap, are zero. When $\beta_2 = 0$, the values of θ and ξ are independent of p, because $\varepsilon_{p,q} = 0$. This means that a_p/a_q and $\phi_p - \phi_q$ are equal to the values obtained without the truncation. In contrast, the truncation causes measurement error when $\beta_2 \neq 0$, because $U_{p,q}$ depends on p. Therefore, we should consider the effect of both truncation and fringe overlap in the presence of β_2.

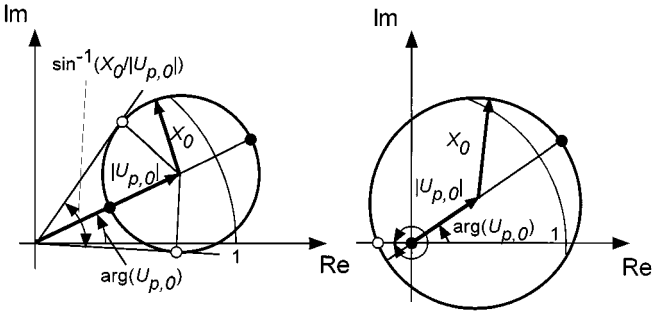

(a) (b)

Fig. 3. Polar diagram of $S'_p(\sigma)/S_p(\sigma)$ for (a) $X_0 \le |U_{p,0}|$ and (b) $X_0 > |U_{p,0}|$.

C. Measurable Limit Due to Second-Order Dispersion

It is important to consider the measurable limit when an error tolerance is given. In this subsection, we first estimate the worst-case measurement errors in phase and amplitude caused by fringe overlap and truncation. Using this knowledge, we then discuss the measurable limit due to second order dispersion.

For simplicity, we use five dominant terms ($q = 0, \pm1, \pm2$) in (13) with approximations $a_{p-q} \simeq a_p$ and $\varepsilon_{p,q} \simeq \varepsilon_{p,0} \equiv \varepsilon_p$ for $q \neq 0$. This does not greatly change the result, because i) $U_{p,q}$ rapidly decreases with increasing $|q|$; ii) a_{p-q} does not differ greatly from those of neighboring paths; iii) ΔL is generally much shorter than L_p in the AWG layout. Under these conditions, $S'_p(\sigma)/S_p(\sigma)$ is given by

$$S'_p(\sigma)/S_p(\sigma) = \sum_{q=0,\pm1,\pm2} |U_{p,q}|\exp(j\Phi_{p,q}) \quad (22)$$

where $\Phi_{p,q} = q\beta(\sigma)\Delta L + (\phi_p - \phi_{p-q}) + \arg(U_{p,q})$ is an unknown phase factor.

The worst-case errors in phase and amplitude become clear when we consider the vector addition of contributions from $|U_{p,0}|\exp(j\Phi_{p,0})$ and $\sum_{q=\pm1,\pm2}|U_{p,q}|\exp(j\Phi_{p,q})$. Fig. 3 shows a polar diagram of $S'_p(\sigma)/S_p(\sigma)$ when $X_0 \le |U_{p,0}|$ and $X_0 > |U_{p,0}|$, where $X_0 = \sum_{q=\pm1,\pm2}|U_{p,q}|$. The value of $S'_p(\sigma)/S_p(\sigma)$ lies within a circle with a radius of X_0 . The open circles in Fig. 3 represent the points at which $\arg[S'_p(\sigma)/S_p(\sigma)]$ is minimum or maximum. The closed circles correspond to the points at which $|S'_p(\sigma)/S_p(\sigma)|$ is maximum or minimum. When $X_0 \le |U_{p,0}|$, the value of θ and $(1+\xi)$ are in the range

$$\Phi_{p,0} - \sin^{-1}\left(\frac{X_0}{|U_{p,0}|}\right) \le (-\theta) \le \Phi_{p,0} + \sin^{-1}\left(\frac{X_0}{|U_{p,0}|}\right) \quad (23)$$

$$|U_{p,0}| - X_0 \le (1+\xi) \le |U_{p,0}| + X_0. \quad (24)$$

Therefore, the worst-case errors $|\theta|_w$ and $|\xi|_w$ are given by

$$|\theta|_w = \min\left[\pi,\ |\Phi_{p,0}| + \sin^{-1}\left(\frac{X_0}{|U_{p,0}|}\right)\right] \tag{25}$$

$$|\xi|_w = |1 - |U_{p,0}|| + X_0 \tag{26}$$

In contrast, when $X_0 > |U_{p,0}|$, we find that $|\theta|_w = \pi$ and $|\xi|_w \geq 1$ as shown in Fig. 3(b).

Equations (25)–(26) indicate that $U_{p,q}$ plays an important role in the worst-case measurement errors. According to (14)–(15), $D^{\pm}_{p,q}$ and $U_{p,q}$ for $\varepsilon_p < 0$ or $\alpha < 0$ follow:

$$D^{\pm}_{p,q}(\chi, \varepsilon_p, -\alpha) = -D^{\mp}_{p,q}(\chi, \varepsilon_p, \alpha)$$
$$D^{\pm}_{p,q}(\chi, -\varepsilon_p, \alpha) = D^{\pm *}_{p,-q}(\chi, \varepsilon_p, \alpha) \tag{27}$$
$$U_{p,q}(\chi, \varepsilon_p, -\alpha) = U_{p,-q}(\chi, \varepsilon_p, \alpha)$$
$$U_{p,q}(\chi, -\varepsilon_p, \alpha) = U^{*}_{p,-q}(\chi, \varepsilon_p, \alpha). \tag{28}$$

These relations indicate that the worst-case errors estimated from (25) to (26) for $\varepsilon_p < 0$ or $\alpha < 0$ are equal to these obtained for $\varepsilon_p > 0$ and $\alpha > 0$. Therefore, we will consider the effect of ε_p and α only in the range $\varepsilon_p \geq 0$ and $\alpha \geq 0$.

Fig. 4 shows contour plots of $|\theta|_w$ and $|\xi|_w$ for $\varepsilon_p = 0$ as a function of χ and α, which is computed from (25) to (26). The error decreases with increasing χ for any α value. Therefore, we can find the minimum value of χ for a given α and an error $|\theta|_w$ (or $|\xi|_w$). Since this relation is unchanged when $\varepsilon_p \neq 0$, we define the minimum χ value by $\chi_{\min} = \chi_{\min}[\alpha, \varepsilon_p, |\theta|_w(\text{or } |\xi|_w)]$. Fig. 5 shows the change in $\chi_{\min}(\alpha, \varepsilon_p, 0.02)$ as a function of α for ε_p ranging from 0 to 2. The value $\chi_{\min}$ must be increased as ε_p increases.

The broken lines in Figs. 4 and 5 show $\chi\alpha = \pi C$ for $C = 0.5$, 1, and 1.5, where $C = (\sigma - \sigma_0)(n_{gr}\Delta L)$ is the parameter related to the wavenumber measurement range. It is effective to use parameter C for comparing measurement errors within the same measurement range. Parameter $C = 1$ means that the wavenumber σ is $\Delta\sigma = 1/(n_{gr}\Delta L)$ apart from σ_0. Since $\Delta\sigma$ is the free spectral range (FSR) of the AWG, there are at least two AWG transmission peaks in the range $|C| \leq 1$.

We have already shown that the $\chi_{\min}$ value is a function of ε_p, $|\theta|_w$ (or $|\xi|_w$) and α (or C). Since $\chi_{\min} \leq \chi = (\pi/\Delta\sigma)\delta\sigma$ and $\varepsilon_p = (|\beta_2|L_p/2)\delta\sigma^2$, we obtain

$$|\beta_2|L_p\Delta\sigma^2 \leq \frac{2\pi^2\varepsilon_p}{\chi^2_{\min}} \tag{29}$$

This means that the maximum value of $2\pi^2\varepsilon_p/\chi^2_{\min}$ determines the upper limit of $|\beta_2|L_p\Delta\sigma^2$. To estimate this value, we first examined the relationship between $\chi_{\min}$ and ε_p. Fig. 6 shows $\chi_{\min}(\alpha, \varepsilon_p, 0.02)$ as a function of ε_p for $|C| \leq 1$. As shown by the broken line in Fig. 6, the maximum value of $\chi_{\min}$ for $|C| \leq 1$ is well approximated by a single function

$$\chi_{\min} \simeq \chi_{\text{fit}}(\varepsilon_p) = \chi_0(1 + \varepsilon_p^2)^{\tau} \tag{30}$$

where χ_0 and τ are fitting parameters ($\tau \simeq 0.5$). This fitting function could be used as an error value ranging from 0.001 to 0.1 with a slight change in χ_0 and τ. Another important feature found from Fig. 6 is that the maximum value of $\chi_{\min}$ for a phase error within $|C| \leq 1$ is almost the same as that for an amplitude error. Therefore, in the following estimation, the use of χ_{fit} implicitly assumes that $|\theta|_w = |\xi|_w$.

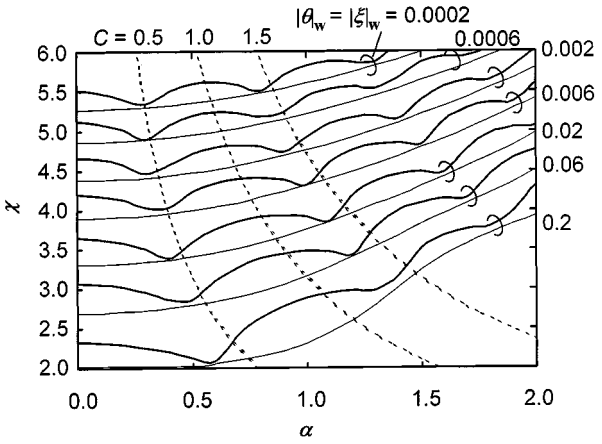

Fig. 4. Contour plots of $|\theta|_w$ (—) and $|\xi|_w$ (- - -) for $\varepsilon_p = 0$ as a function of χ and α. The broken lines show $\chi\alpha = \pi C$, where $C = (\sigma - \sigma_0)n_{gr}\Delta L$.

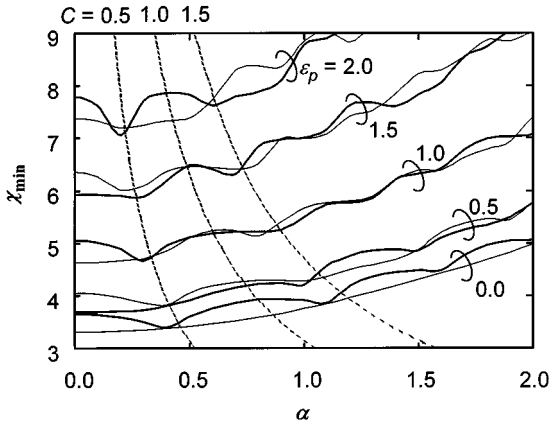

Fig. 5. $\chi_{\min}$ as a function of α for $\varepsilon_p = 0,\ 0.5,\ 1.0,\ 1.5$ when $|\theta|_w = 0.02$ (—), $|\xi|_w = 0.02$ (- - -).

Using (30), we then calculated the value of $2\pi^2\varepsilon_p/\chi^2_{\min}$ ($= 2\pi^2\varepsilon_p/\chi^2_{\text{fit}}$) as a function of ε_p for different error values. The result are shown in Fig. 7. The value of $2\pi^2\varepsilon_p/\chi^2_{\text{fit}}$ has a peak near $\varepsilon_p = 1.1$ and the peak value decreases with the decreasing error value. Fig. 8 shows the peak values of $2\pi^2\varepsilon_p/\chi^2_{\text{fit}}(\varepsilon_{\text{peak}})$ and $\chi_{\text{fit}}(\varepsilon_{\text{peak}})$, where $\varepsilon_{\text{peak}}$ is the value of ε_p for which $2\pi^2\varepsilon_p/\chi^2_{\text{fit}}$ has a peak value. The maximum measurable value of $|\beta_2|L_p\Delta\sigma^2$ in the presence of $|\beta_2|$ can be read from this figure for an allowable error from 0.001 to 0.1.

In the last part of this section, we estimate the maximum measurable length for a given $|\beta_2|$ and $\Delta\sigma$ using the obtained maximum value of $2\pi^2\varepsilon_p/\chi^2_{\min}$. The criterion for this estimation is that the errors of $|\theta|_w$ and $|\xi|_w$ are less than or equal to 0.02. We selected this criterion because the value of 0.02 rad is close to the typical value of phase measurement error caused by noise. The criterion determines $2\pi^2\varepsilon_p/\chi^2_{\text{fit}}(\varepsilon_{\text{peak}}) = 0.68$ and $\chi_{\text{fit}}(\varepsilon_{\text{peak}}) = 5.8$. Under these conditions, we calculate the maximum measurable length for an FSR of $c\Delta\sigma = 6.4,\ 3.2,\ 1.6$ THz, where c is the velocity of light in a vacuum.

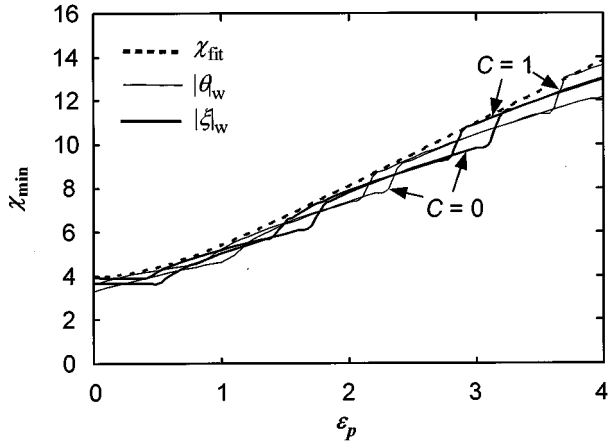

Fig. 6. $\chi_{\min}$ as a function of ε_p for $C = 0, 1$.

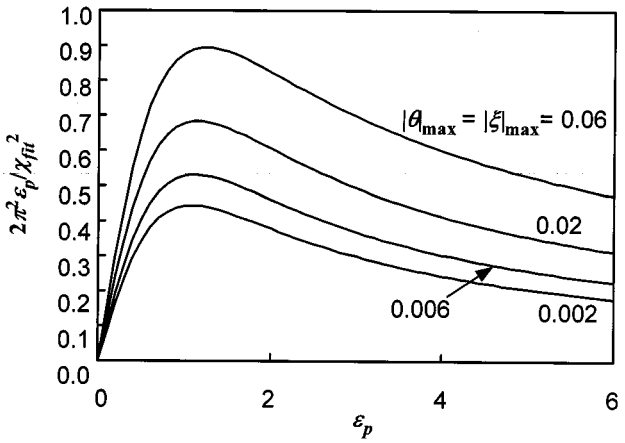

Fig. 7. Relationship between ε_p and $2\pi^2\varepsilon_p/\chi_{\rm fit}^2$.

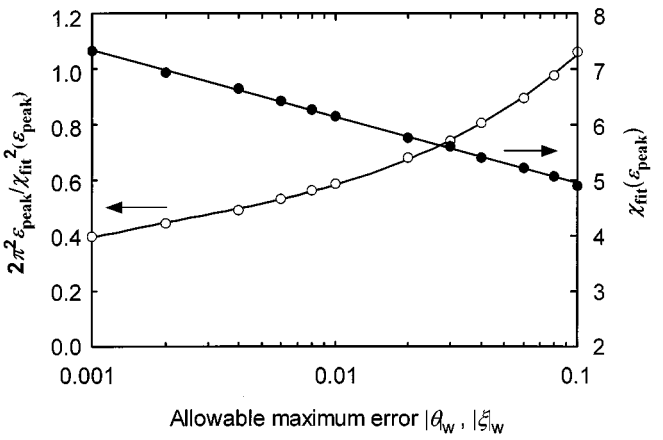

Fig. 8. $2\pi^2\varepsilon_p/\chi_{\rm fit}^2(\varepsilon_{\rm peak})$ and $\chi_{\rm fit}(\varepsilon_{\rm peak})$ as a function of allowable maximum error $|\theta|_w$, $|\xi|_w$, where $\varepsilon_{\rm peak}$ is the ε_p value for which $2\pi^2\varepsilon_p/\chi_{\rm fit}^2(\varepsilon_p)$ has the maximum value.

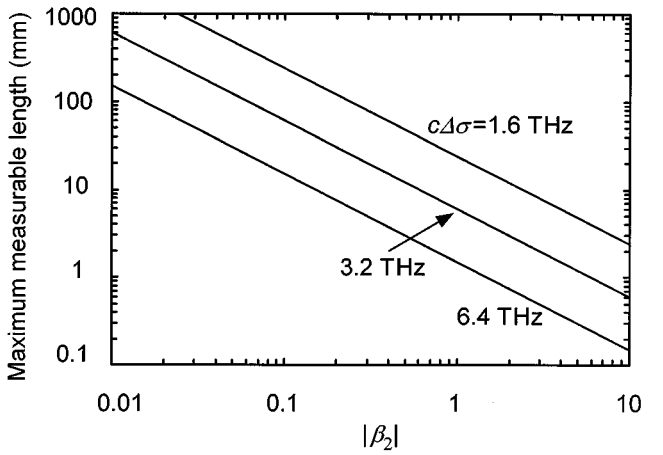

Fig. 9. Maximum measurable length versus $|\beta_2|$ for an AWG whose FSR $c\Delta\sigma = 6.4, 3.2$, and 1.6 THz.

The results are shown as a function of $|\beta_2|$ (Fig. 9). If the maximum path length in an AWG exceeds the length shown in this graph, we need to reduce the effect of GVD using one of the methods shown in the next section.

III. Interferogram Restoration to Reduce Measurement Error

A. Balance Method

A simple method for reducing the effect of the GVD in the waveguide is to balance the dispersion of the reference arm with that of the measurement arm ($\beta(\sigma)L$) in the interferometer. This is possible by using either a computational approach in which $\beta(\sigma)L$ is added to the phase term in the middle of (2) or an experimental approach in which a waveguide with the same dispersion and length is placed in the reference arm. The resultant interferogram is given by (3) with a difference that $L_p = [p - (M-1)/2]\Delta L$. If this balance method provides sufficiently separated fringe patterns, we can obtain the transfer function for the pth path as

$$S_p(\sigma) = a_p(\sigma)\exp[-j\psi_p(\sigma)] \tag{31}$$

where

$$\psi_p(\sigma) = \phi_p + \beta(\sigma)[p - (M-1)/2]\Delta L \tag{32}$$

Thus, the balance method is equivalent to reducing the path length L_p of the AWG.

Although this method eliminates the dispersion at a particular path where $x \simeq n_{gr}L$, the dispersion effect still exists at the other paths. The maximum measurement error for this balance method occurs for a path whose index $p = 0$ or $M-1$. Using (30), we obtain

$$|\beta_2|\left(\frac{M-1}{2}\Delta L\right)\Delta\sigma^2 \le \frac{2\pi^2\varepsilon_p}{\chi_{\rm fit}^2(\varepsilon_p)}. \tag{33}$$

The condition for the number of arrays M can be written as

$$M \le 1 + \frac{2\pi^2\varepsilon_p}{\chi_{\rm fit}^2(\varepsilon_p)}\left(\frac{2n_{gr}}{|\beta_2|}\right)\frac{1}{\Delta\sigma} \tag{34}$$

Thus, the maximum measurable number of arrays decreases with increasing FSR $\Delta\sigma$. Another useful form of the measurable condition results from representing the number of arrays

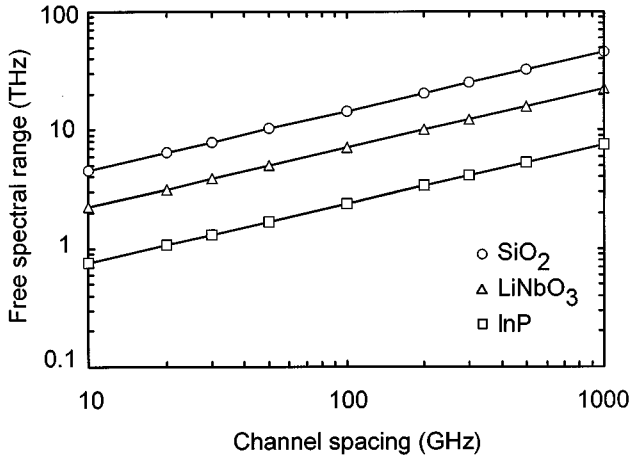

Fig. 10. Maximum measurable FSR versus channel spacing of an AWG for several materials when the maximum allowable measurement error $|\theta|_w = |\xi|_w = 0.02$.

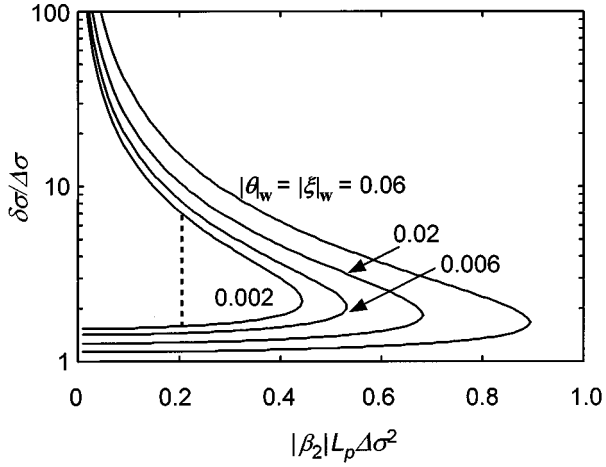

Fig. 11. Required condition for the spectral width of a light source as a function of $|\beta_2|L_p\Delta\sigma^2$. For the balance method, $L_p = [p-(M-1)/2]\Delta L$ and for wavenumber scale transformation $|\beta_2| = 0$. The broken line shows the range of spectral width where the maximum measurement error $|\theta|_w = |\xi|_w \leq 0.002$.

TABLE I
GROUP INDEXES n_{gr}, DISPERSION β_2 FOR DIFFERENT MATERIALS AT DIFFERENT WAVELENGTHS

Material	$\lambda_0[\mu m]$	$n_{\rm gr}$	$\beta_2[\mu m]$
SiO_2 [a]	1.500	1.46	-0.06
$LiNbO_3$ [a]	1.400	2.19	0.5
InP [b]	1.535	3.4	6.8

a. from ref. [24]

b. obtained in this article (section V)

TABLE II
AWG DESIGN PARAMETER

		A	B
Channel spacing	$c\Delta\sigma_{\rm ch}$	50 GHz	200 GHz
Free spectral range	$c\Delta\sigma$	3.2 THz	1.6 THz
Number of array	M	232	28

M in terms of a parameter $M_N = (M-1)/N$, where $N = \Delta\sigma/\Delta\sigma_{ch}$ is the available maximum number of channels in the AWG. We can thus rewrite (34) as

$$\Delta\sigma \leq \sqrt{\frac{2\pi^2\varepsilon_p}{\chi^2_{\rm fit}(\varepsilon_p)}\left(\frac{n_{gr}}{|\beta_2|}\right)\left(\frac{2}{M_N}\right)}\,\Delta\sigma_{ch} \tag{35}$$

Fig. 10 shows the maximum measurable FSR $c\Delta\sigma$ as a function of channel spacing for several waveguide materials under the assumption that $M_N = 3.6$ and $2\pi^2\varepsilon_p/\chi^2_{\rm fit} = 0.68$ ($|\theta|_w = |\xi|_w = 0.02$). The dispersion parameters for waveguide materials used for calculation is listed in Table I. For SiO_2- and $LiNbO_3$-based AWGs, $c\Delta\sigma = 7$ THz ($N = 70$) for $c\Delta\sigma_{ch} = 100$ GHz and $c\Delta\sigma = 5$ THz ($N = 100$) for $c\Delta\sigma_{ch} = 50$ GHz are the limit of the FSR (N) to measure within an allowable error of less than 0.02. Since the FSR of almost all AWGs satisfies the above condition, this balance method can be employed for SiO_2- and $LiNbO_3$-based AWGs. In contrast, an InP-based AWG whose FSR of $c\Delta\sigma > 2.4$ THz ($N > 24$) for $c\Delta\sigma_{ch} = 100$ GHz or $c\Delta\sigma > 1.7$ THz ($N > 34$) for $c\Delta\sigma_{ch} = 50$ GHz cannot be measured within the same error tolerance.

B. Wavenumber Scale Transformation Method

Another way to reduce the effect of the GVD in the waveguide is to use a numerical algorithm. This method is based on a wavenumber scale transformation [23], [24], where

$$\nu = \sigma + [\beta(\sigma) - \beta_0 - \beta_1(\sigma-\sigma_0)]/\beta_1 = \zeta(\sigma)$$
$$\tilde{G}(\nu)\tilde{H}(\nu) = G[\zeta(\sigma)]H[\zeta(\sigma)]. \tag{36}$$

Fourier transform in terms of the new wavenumber ν gives a restored interferogram

$$\begin{aligned}\tilde{I}(x) &= \int_{-\infty}^{\infty}\tilde{G}(\nu)\tilde{H}(\nu)\exp(j2\pi x\nu)\,d\nu \\ &= \int_{-\infty}^{\infty}\tilde{G}(\nu)\sum_{p=0}^{M-1}a_p e^{-j\phi_p}\exp(j2\pi x\nu) \\ &\quad\times\exp\{-j[\beta_0+\beta_1(\nu-\nu_0)]L_p\} \\ &= \sum_{p=0}^{M-1}\tilde{I}_p(x).\end{aligned} \tag{37}$$

This restored interferogram is the same that obtained by measuring a nondispersive waveguide. If the restored fringe is sufficiently separated from the neighboring fringes, the transfer function for pth path can be approximated as

$$\tilde{S}_p(\nu) = \tilde{a}_p(\nu)\exp[-j\tilde{\psi}_p(\nu)]. \tag{38}$$

where

$$\tilde{\psi}_p(\nu) = \tilde{\phi}_p + [\beta_0 + \beta_1(\nu - \nu_0)]L_p \tag{39}$$

Thus, this method is equivalent to reducing the higher order dispersion $\beta_k = (d^k\beta/d\sigma^k)$ $(k = 2, 3\ldots)$.

The measurement error in $\tilde{\phi}_p(\nu)$ and $\tilde{a_p}(\nu)$ estimated from the Fourier transform of $\tilde{I}_p(x)$ is no longer affected by the GVD in the waveguide. Although this method requires knowledge of the waveguide dispersion parameter and a more complicated calculation than the balance method, there is no restriction on the channel number or channel spacing of the AWG under test. Therefore, (35) can be used as a criterion, when we select a restoration method.

C. Required Condition for Spectral Width of Light Source

In the preceding subsections, we showed that either or both restoration techniques can reduce the effective value of $|\beta_2|L_p$ to satisfy the condition as in (29). We recall it by rewriting it as

$$|\beta_2|L_p\Delta\sigma^2 \le \frac{2\pi^2\varepsilon_p}{\chi^2_{\rm fit}(\varepsilon_p)} \tag{40}$$

Since the value of the left-hand side in (40) is determined when the restoration method is selected, we can obtain the condition for χ for a given allowable error by using (30) and (40). It cannot be solved analytically, however, it is generally written as $\chi_0 \le \chi_1 \le \chi \le \chi_2$, where χ_1 and χ_2 are, respectively, the allowable minimum and maximum values of χ and are a function of $|\beta_2|L_p\Delta\sigma^2$. Finally, the condition for the spectral width $\delta\sigma$ of a light source is given by

$$\frac{\chi_0}{\pi} \le \frac{\chi_1}{\pi} \le \frac{\delta\sigma}{\Delta\sigma} \le \frac{\chi_2}{\pi}. \tag{41}$$

For the special case where $\beta_2 = 0$, $\chi_1 = \chi_0$ and $\chi_2 = \infty$.

Fig. 11 shows the condition for $\delta\sigma/\Delta\sigma$ as a function of $|\beta_2|L_p\Delta\sigma^2$. The broken line in Fig. 11 shows an example of the range of $\delta\sigma/\Delta\sigma$ for $|\beta_2|L_p\Delta\sigma^2 = 0.2$ and $|\theta|_w = |\xi|_w = 0.002$. As the figure shows, the range of $\delta\sigma/\Delta\sigma$ decreases with increasing $|\beta_2|L_p\Delta\sigma^2$ value and the widest tolerance for selecting the $|\beta_2|L_p\Delta\sigma^2$ value can be found when $\delta\sigma/\Delta\sigma \simeq 2$. Another important feature of the condition is that an AWG with a wider FSR requires a light source with a wider spectral width.

We have derived the required conditions for the dispersion parameter $|\beta_2|$, path length L_p, FSR $\Delta\sigma$ and spectral width $\delta\sigma$ for the AWG measurement. We believe that the derived conditions can easily be extended to the measurement of other types of linear circuits which do not include recursive circuits such as distributed Bragg gratings, ring resonators and Fabry–Perot interferometers.

IV. Experimental Results

We show the results of experimental phase and amplitude distribution measurements undertaken using the restoration methods mentioned in the preceding section. The devices under test were two types of InP-based AWG [14], [15]. Table II lists the parameters of these AWGs. For the distribution measurements, we used a fiber-optic MZI [10]. For the coupling of the light into the InP-based AWG, we used two lensed fibers. The light source was a super luminescent diode with $\delta\sigma = 2.3\times10^4$ m^{-1} ($c\delta\sigma = 6.9$ THz) and a center wavelength of 1535 nm. We have $\delta\sigma/\Delta\sigma = 2.2$ for the 50 GHz AWG and $\delta\sigma/\Delta\sigma = 4.3$ for the 50-GHz AWG.

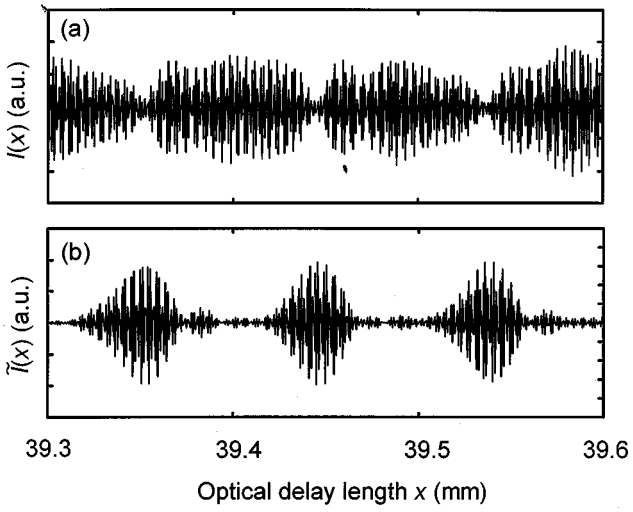

Fig. 12. Part of an interferogram for a 50-GHz AWG (a) before and (b) after wavenumber scale transformation.

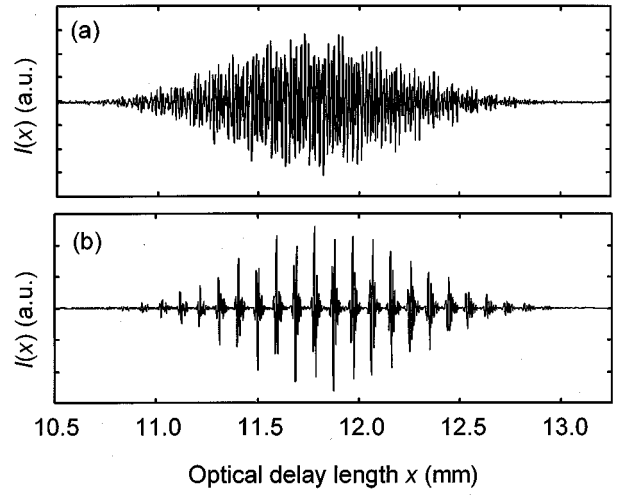

Fig. 13. Interferogram for a 200-GHz AWG (a) before and (b) after applying the balance method.

Figs. 12(a) and 13(a) show measured interferograms for the AWGs with channel spacings of 50 and 200 GHz, respectively. The fringes of both interferograms overlapped, thus preventing us from obtaining isolated fringes. To allow us to choose a suitable interferogram restoration method, we measured the transfer function of a reference waveguide using Fourier transform spectroscopy. The phase of the transfer function was fitted with the function given by (8). Then the dispersion parameters were determined as $n_{gr} = 3.4$ and $\beta_2 = 6.8$ μm. These values were used to calculate the measurable maximum FSR for $|\theta|_w = |\xi|_w = 0.02$ when the balance method is applied.

Since the maximum measurable FSR for the 50-GHz AWG was 1.68 THz, which is smaller than the FSR of 3.2 THz,

we used a wavenumber scale transformation to reduce the effect of second order dispersion in the interferogram. We calculated the value of $G(\sigma)H(\sigma)$ for $\sigma = \zeta^{-1}(\nu_0 + k\Delta\nu)$ ($k = \pm1, \pm2, \pm3\ldots$) using a discrete Fourier transform. Then we obtained $\tilde{I}(x)$ using a fast Fourier transform (FFT) with respect to the ν scale.

In contrast, we used the balance method for the 200 GHz AWG, because the measurable maximum FSR was 3.48 THz and this is larger than the FSR of 1.6 THz. We calculated the $G(\sigma)H(\sigma)$ value using an FFT and added $\beta(\sigma)L$ to its phase term. Then we obtained a restored interferogram using an FFT.

Figs. 12(b) and 13(b) show the restored interferogram for the 50 and 200 GHz AWGs, respectively. We successfully obtained isolated fringe patterns. Although the balance method did not completely remove the effect of the second order dispersion near the edge of the array [Fig. 13(b)], the fringes were well separated because of the long path difference ΔL of the 200 GHz AWG.

Fig. 14(a) and (b) show the amplitude and phase error distributions calculated from the restored interferogram for the 50 and 200 GHz AWGs, respectively. We obtained ϕ_p and a_p ($p =$ 19–214) for the 50 GHz AWG and ($p = 2$–25) for the 200 GHz AWG. The phase and amplitude of the other waveguides could not be measured because of noise. The effect of these errors on the AWG performance will be discussed in Section V.

We consider here the accuracy with which ϕ_p and a_p were measured. For this purpose, we calculated the transmission spectra $T^{(e)}(\sigma)$ from the phase and amplitude distributions and $T^{(i)}(\sigma)$ from $I(x)$ (Fig. 15). In the calculation of $T^{(e)}(\sigma)$, $\psi_p(\sigma)$ given by (31) was used for the 200 GHz AWG to include the effect of GVD. For the 50 GHz AWG, $\tilde{H}(\nu)$ was calculated from $\tilde{\psi}_p(\nu)$ and $\tilde{a_p}(\nu)$. Then we converted the wavenumber scale ν to σ so that $H(\sigma) = \tilde{H}(\zeta(\sigma))$ and obtained $T^{(e)}(\sigma)$. The agreement of $T^{(i)}(\sigma)$ and $T^{(e)}(\sigma)$ shows that we obtained ϕ_p and a_p without serious deformation during the interferogram restoration.

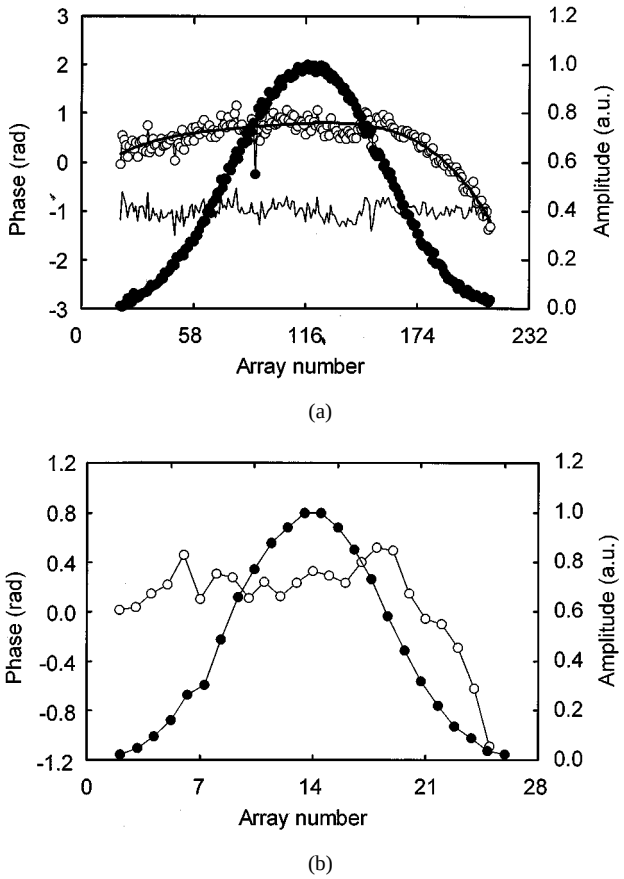

Fig. 14. Phase and amplitude distributions for (a) 50 GHz AWG and (b) 200 GHz AWG.

V. Crosstalk and Dispersion in an AWG Based on a Dispersive Waveguide

A. Crosstalk

Here we discuss the crosstalk in an AWG based on a dispersive waveguide using the expression of the AWG transfer function

$$H(\sigma) = \exp[-j\beta(\sigma)L]T(\sigma) \tag{42}$$

where

$$T(\sigma) = \sum_{p=0}^{M-1} a_p \exp(-j\phi_p) \times \exp\left[-j\beta(\sigma)\left(p - \frac{M-1}{2}\right)\Delta L\right]. \tag{43}$$

With a wavenumber scale transformation given by (36), we obtain

$$\tilde{T}(\nu) = \sum_{p=0}^{M-1} a_p \exp(-j\phi_p) \times \exp\left\{-j[\beta_0 + \beta_1(\nu - \nu_0)] \cdot \left(p - \frac{M-1}{2}\right)\Delta L\right\} \tag{44}$$

These relations shows that the maximum crosstalk level of the AWG is independent of $\beta(\sigma)$, because $|T(\sigma)|^2 = |\tilde{T}[\zeta(\sigma)]|^2$. Thus, the maximum crosstalk of the AWG based on a dispersive waveguide is determined only by the phase and amplitude distributions. The effect of $\beta(\sigma)$ on the AWG amplitude response is related to the change in the wavenumber scale from σ into ν, which causes the change in, for example, the FSR and peak wavelength.

To examine the effect of phase error on the crosstalk in the 50-GHz InP-based AWG, we divided the phase error distribution into random $\phi_p^{(r)}$ and slowly-varying $\phi_p^{(s)}$ components. Here $\phi_p^{(r)}$ and $\phi_p^{(s)}$ correspond to Fourier components whose order is $r \geq 4$ and $r < 4$, respectively. These are shown as the light and heavy lines in Fig. 14(a). The transmission spectrum assuming $\phi_p^{(r)} = 0$ was calculated and is shown as the broken line in Fig. 15(a). This reveals that the main origin of the crosstalk is random phase error with an rms of 0.16 rad. The broken line in Fig. 15(b) shows the transmission spectrum of the 200 GHz AWG when there are no phase errors ($\phi_p = 0$). The crosstalk was also caused by phase error in the 200-GHz AWG. These results are the same as found with SiO_2-based AWGs [9]–[11].

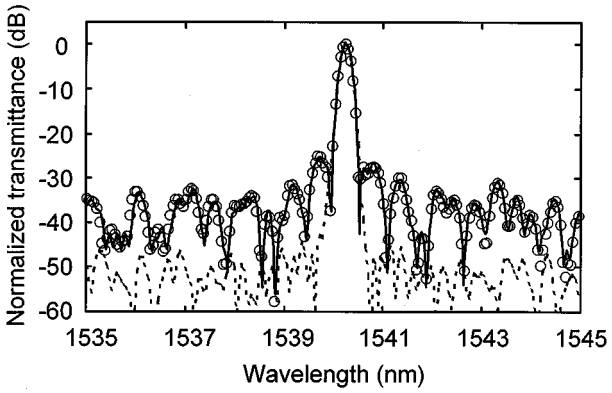

(a)

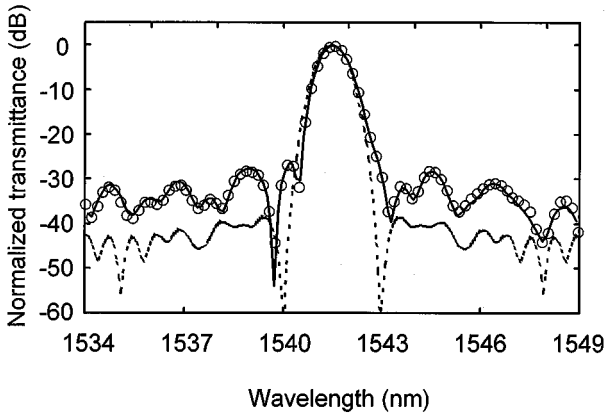

(b)

Fig. 15. Transmission spectrum for (a) 50 GHz AWG and (b) 200 GHz AWG. ($\circ$: $|T^{(i)}(\sigma)|^2$; — : $|T^{(e)}(\sigma)|^2$; - - - : $|T^{(e)}(\sigma)|^2$ assuming (a) $\phi_p^{(r)} = 0$ and (b) $\phi_p = 0$)

B. Chromatic Dispersion

The AWG dispersion consists of the GVD of the AWG central path and multipath interference dispersion, which are, respectively, related to $\beta(\sigma)L$ and $\Psi(\sigma) = -\arg[T(\sigma)]$ as shown in (42)–(43). The group delay $\tau(\sigma)$ and the dispersion $D(\sigma)$ can be expressed as

$$\tau(\sigma) = \tau^{(m)}(\sigma) + \tau^{(g)}(\sigma) = \left(\frac{1}{2\pi c}\right)\left(\frac{d\Psi}{d\sigma}\right) + \left(\frac{1}{2\pi c}\right)\left(\frac{d\beta}{d\sigma}\right)L \quad (45)$$

$$D(\sigma) = D^{(m)}(\sigma) + D^{(g)}(\sigma) = \left(\frac{-\sigma^2}{2\pi c}\right)\left(\frac{d^2\Psi}{d\sigma^2}\right) + \left(\frac{-\sigma^2}{2\pi c}\right)\left(\frac{d^2\beta}{d\sigma^2}\right)L \quad (46)$$

where the superscript (m) indicates its relation to the multipath interference and (g) to the GVD.

When there are no phase or amplitude errors, $\tau^{(m)}(\sigma) = D^{(m)}(\sigma) = 0$ regardless of $\beta(\sigma)$. The reason is that the transfer function can be written as

$$T(\sigma) = \sum_{p=0}^{M-1} a_p \cos\left[\beta(\sigma)\left(p - \frac{M-1}{2}\right)\Delta L\right] \quad (47)$$

and then has a real value. However, in a practical AWG, there are phase and amplitude errors, which lead to nonzero values of $\tau^{(m)}(\sigma)$ and $D^{(m)}(\sigma)$. The values of $\tau^{(m)}(\sigma)$ and $D^{(m)}(\sigma)$, as well as those of $\tau^{(d)}(\sigma)$ and $D^{(d)}(\sigma)$, depend on $\beta(\sigma)$ unlike the maximum crosstalk.

In order to consider the effect of $\beta(\sigma)$ on $\tau^{(m)}(\sigma)$ and $D^{(m)}(\sigma)$, it is useful to rewrite the first and second derivatives of $\Psi(\sigma)$ by using $\tilde{\Psi}(\nu) = -\arg[\tilde{T}(\nu)]$. This is because $\tilde{\Psi}(\nu)$ is the same as the value we would obtain for a nondispersive waveguide, as shown in (44). The results are given by

$$\frac{d\Psi}{d\sigma} = \frac{d\tilde{\Psi}}{d\nu}\left(\frac{1}{\beta_1}\frac{d\beta}{d\sigma}\right) \quad (48)$$

$$\frac{d^2\Psi}{d\sigma^2} = \frac{d^2\tilde{\Psi}}{d\nu^2}\left(\frac{1}{\beta_1}\frac{d\beta}{d\sigma}\right)^2 + \frac{d\tilde{\Psi}}{d\nu}\left(\frac{1}{\beta_1}\frac{d^2\beta}{d\sigma^2}\right) \quad (49)$$

where we use the relation $d\nu/d\sigma = (1/\beta_1)(d\beta/d\sigma)$.

In the terms of the phase response, it is sufficient to consider the σ range where $|\sigma - \sigma_c|$ is less than the channel spacing of the AWG, where σ_c is the center wavenumber of the passband. For an AWG whose channel spacing is less than 200 GHz, $|\sigma - \sigma_c| < 6.7\times10^{-4}\ \mu\text{m}^{-1}$. Using this knowledge and neglecting β_k ($k = 3, 4\ldots$), we obtain $(1/\beta_1)(d\beta/d\sigma) \simeq 1 + (\beta_2/\beta_1)(\sigma_c - \sigma_0)$ and $(1/\beta_1)(d^2\beta/d\sigma^2) \simeq (\beta_2/\beta_1)$. When $\sigma_c - \sigma_0$ is negligible, we can approximate $\tau^{(m)}(\sigma)$ and $D^{(m)}(\sigma)$ as

$$\tau^{(m)}(\sigma) \simeq \tilde{\tau}^{(m)}[\zeta(\sigma)] \quad (50)$$

$$D^{(m)}(\sigma) \simeq \tilde{D}^{(m)}[\zeta(\sigma)] - (\beta_2/\beta_1)\nu^2\tilde{\tau}^{(m)}[\zeta(\sigma)] \quad (51)$$

where

$$\tilde{\tau}^{(m)}(\nu) = (1/2\pi c)(d\tilde{\Psi}/d\nu) \quad (52)$$

$$\tilde{D}^{(m)}(\nu) = (-\nu^2/2\pi c)(d^2\tilde{\Psi}/d\nu^2). \quad (53)$$

Since $(\beta_2/\beta_1)\nu^2 < 10^{-3}\ \text{nm}^{-1}$ when $\nu < 1\ \mu\text{m}^{-1}$ and $\beta_2/\beta_1 < 1\ \mu$m, the contribution of the term $(\beta_2/\beta_1)\nu^2\tilde{\tau}^{(m)}(\nu)$ to (51) is as small as less than 0.1 ps/nm even if there is a large group delay $\tilde{\tau}^{(m)}(\nu) = 100$ ps. Thus, we can approximate $D^{(m)}(\sigma) = \tilde{D}^{(m)}[\zeta(\sigma)]$ unless $\tilde{\tau}^{(m)}(\nu)$ expressed in picosecond units is 10^3 times larger than $\tilde{D}^{(m)}(\nu)$ in ps/nm units.

The use of the neglected term $(\sigma_c - \sigma_0)$ in $(1/\beta_1)(d\beta/d\sigma)$ gives the dependence of $\tau^{(m)}(\sigma)$ [or $D^{(m)}(\sigma)$] on the channel or wavenumber at which the AWG is measured. When we assume that the deformation of the phase and amplitude distributions occurs only, as in typical cases, at the arrayed-waveguides, the error distributions are independent of channel. In this case, the values of $\tilde{\tau}^{(m)}(\nu)$ [or $\tilde{D}^{(m)}(\nu)$] for different channels are almost the same. Thus, the fractional difference of $\tau^{(m)}(\sigma)$ [or $D^{(m)}(\sigma)$] between two channels is given by

$$\frac{\tau^{(m)}(\sigma_{c1}) - \tau^{(m)}(\sigma_{c2})}{\tau^{(m)}(\sigma_0)} \simeq (\beta_2/\beta_1)(\sigma_{c1} - \sigma_{c2}) \quad (54)$$

$$\frac{D^{(m)}(\sigma_{c1}) - D^{(m)}(\sigma_{c2})}{D^{(m)}(\sigma_0)} \simeq (2\beta_2/\beta_1)(\sigma_{c1} - \sigma_{c2}) \quad (55)$$

where σ_{c1} and σ_{c2} are the center wavenumbers for two channels. Even if $c(\sigma_{c1} - \sigma_{c2}) = 10$ THz, the dispersion difference $(2\beta_2/\beta_1)(\sigma_{c1} - \sigma_{c2})$ is 2.1% for $\beta_2/\beta_1 = 0.32\ \mu$m. Therefore, we can consider that $\tau^{(m)}(\sigma)$ and $D^{(m)}(\sigma)$ are independent of the channel or wavenumber at which the AWG is measured.

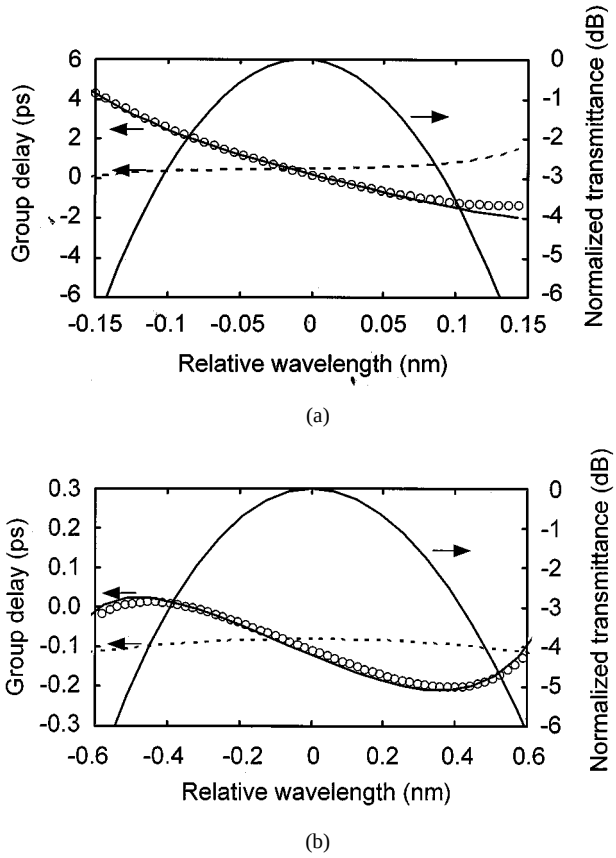

Fig. 16. Group delay for (a) 50 GHz AWG and (b) 200 GHz AWG. [o : $\tau(\sigma)$; — : $\bar{\tau}^{(m)}(\sigma)$; - - - : $\bar{\tau}^{(m)}(\sigma)$ assuming (a) $\phi_p^{(s)} = 0$ and (b) $\phi_p = 0$]

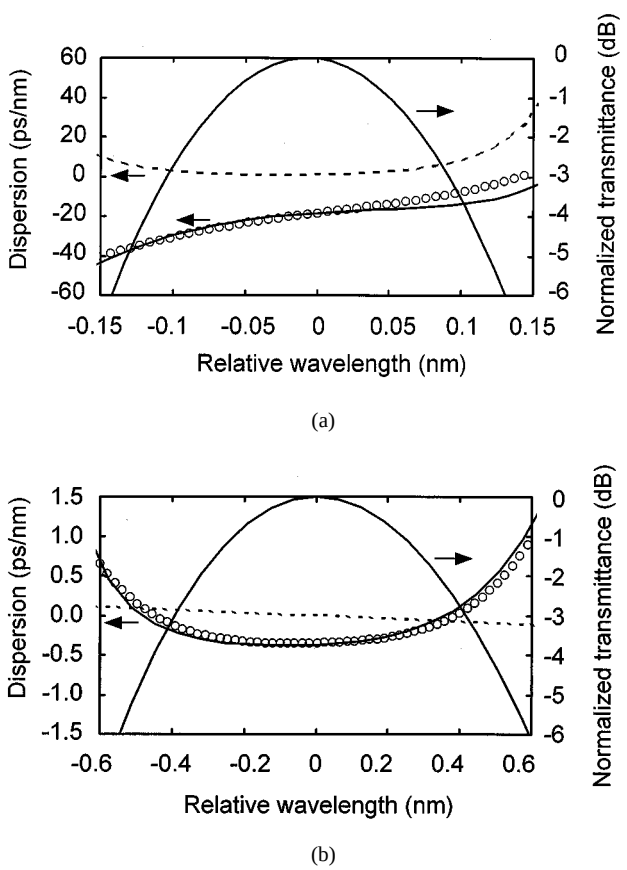

Fig. 17. Dispersion for (a) 50 GHz AWG and (b) 200 GHz AWG. [o : $D(\sigma)$; — : $\bar{D}^{(m)}(\sigma)$; - - - : $\bar{D}^{(m)}(\sigma)$ assuming (a) $\phi_p^{(s)} = 0$ and (b) $\phi_p = 0$]

Using the above knowledge, we discussed the dispersion in InP-based AWGs. Fig. 16 shows the calculated group delay for 50 and 200 GHz AWGs. The open circles show $\tau(\sigma)$ obtained from an FFT of the interferogram [25]–[27]. The phase $\Psi(\sigma)$ was calculated and approximated by a power series expansion about the point $\sigma = \sigma_c$ to order $(\sigma - \sigma_c)^6$. Then, we used the expansion coefficients to calculate the first and second derivatives of $\Psi(\sigma)$. The solid line shows $\tilde{\tau}^{(m)}(\nu)$ calculated using the distributions of $a_p(\sigma_c)$ and $\phi_p(\sigma_c)$ and (52)–(53). The agreement of $\tau(\sigma)$ and $\tilde{\tau}^{(m)}(\nu)$ shows that the effect of GVD on the estimation of $\tau(\sigma)$ is negligible. This result agrees well with that mentioned above. Since the calculated $\tau(\sigma)$ contains $\tau^{(g)}(\sigma)$, the results also show that $\tau^{(g)}(\sigma)$ is negligibly smaller than $\tau^{(m)}(\sigma)$. This result is reasonable because the estimated value of $\tau^{(g)}(\sigma)$ is -6.1×10^{-2} ps/nm for the 50 GHz AWG and -4.3×10^{-2} ps/nm for the 200 GHz AWG. As Fig. 17 shows, we were also able to evaluate the dispersion $D(\sigma)$ both from an FFT of the interferogram and from the phase and amplitude distributions.

Finally, we examined the effect of phase error on the group delay and dispersion [12]. For this purpose, we calculated $\tilde{\tau}^{(m)}(\sigma)$ and $\tilde{D}^{(m)}(\sigma)$ assuming $\phi_p^{(s)} = 0$ for the 50 GHz AWG. The results are shown as the broken lines in Figs. 16(a) and 17(a). This shows that the slowly-varying phase error is the main origin of the dispersion. This feature is the same as that found with SiO_2-based AWGs [12]. For the 200 GHz AWG, the group delay and dispersion were calculated assuming $\phi_p = 0$ and are also shown as the broken lines in Figs. 16(b) and 17(b). As with the 50 GHz AWG, the group delay for the 200 GHz AWG was caused by phase error.

VI. Conclusion

We accurately measured the phase and amplitude distributions in InP-based AWGs through the use of Fourier transform spectroscopy with a low-coherence interferometer in combination with an interferogram restoration technique (balance method or wavenumber scale transformation). We estimated the worst-case measurement error caused by fringe overlap and truncation to clarify the measurable limit in the presence of second order dispersion. The results showed that: 1) the worst-case measurement error in phase expressed in units of radians and that in fractional amplitude within the same measurement range were almost the same and 2) the product of second order dispersion $|\beta_2|$ and path length L_p in the AWG must be less than 0.68, when we require that the worst-case measurement errors in phase and amplitude are less than 0.02. We showed that one or both of the interferogram restoration methods can reduce the measurement error to within a given tolerance, regardless of the $|\beta_2|L_p$ value. This is because, the balance method can reduce the effective value of L_p to $\Delta L(M-1)/2$ and wavenumber scale transformation can reduce the effective value of $|\beta_2|$ to 0 when the $|\beta_2|$ value is known. We obtained a criterion to allow us to choose a suitable interferogram restoration method. This criterion is

the maximum measurable FSR of the AWG with the balance method, shown as a function of channel spacing and $|\beta_2|$.

Using this knowledge, we selected one of the interferogram restoration methods for the measurement of 50 and 200 GHz InP-based AWGs. After employing the selected technique, we successfully obtained the phase and amplitude distributions. The measured distributions in phase and amplitude revealed that the main origin of the crosstalk and dispersion in InP-based AWGs is phase error. This feature of phase error in InP-based AWGs was the same as that found with SiO_2-based AWGs [11], [12]. We believe that Fourier transform spectroscopy with a low-coherence interferometer and interferogram restoration techniques will play an important role in the improvement of the crosstalk and dispersion in AWGs based on dispersive waveguides.

ACKNOWLEDGMENT

The authors would like to thank Y. Yoshikuni for his valuable advice and encouragement.

REFERENCES

[1] M. K. Smit, "New focusing and dispersive planar component based on an optical phased array," *Electron. Lett.*, vol. 24, pp. 385–386, 1988.

[2] C. Dragone, C. A. Edwards, and R. C. Kistler, "Integrated optics $N \times N$ multiplexer on silicon," *IEEE Photon. Technol. Lett.*, vol. 3, pp. 896–899, 1991.

[3] H. Takahashi, S. Suzuki, and I. Nishi, "Multi/demultiplexer for nanometer-spacing WDM using arrayed-waveguide grating," in *Proc. IPR'91*, Monterey, CA, 1991, Postdeadline Paper PD-1-1.

[4] M. K. Smit and C. van Dam, "Phaser-based WDM-devices: Principle, design and application," *IEEE J. Select. Topics Quantum Electron.*, vol. 2, pp. 236–250, 1996.

[5] K. Okamoto, "Recent progress of integrated optics planar lightwave circuits," *Opt. Quantum Electron.*, vol. 31, pp. 107–129, 1999.

[6] H. Yamada, K. Takada, Y. Inoue, Y. Hibino, and M. Horiguchi, "10GHz-spaced arrayed-waveguide grating multiplexer with phase-error-compensating thin-film heaters," *Electron. Lett.*, vol. 30, pp. 360–361, 1995.

[7] H. Yamada, K. Takada, Y. Inoue, Y. Ohmori, and S. Mitachi, "Statically-phase-compenated 10 GHz spaced arrayed-waveguide grating," *Electron. Lett.*, vol. 32, pp. 1580–1582, 1996.

[8] H. Yamada, K. Takada, Y. Inoue, K. Okamoto, and S. Mitachi, "Low-crosstalk arrayed-waveguide grating multi/demultiplexer with phase compensating plate," *Electron. Lett.*, vol. 33, pp. 1698–1699, 1997.

[9] K. Takada, Y. Inoue, H. Yamada, and M. Horiguchi, "Measurement of the phase error distribution in silica-based arrayed-waveguide grating multiplexers by using Fourier transform spectoroscopy," *Electron. Lett.*, vol. 30, pp. 1671–1672, 1994.

[10] K. Takada, H. Yamada, and Y. Inoue, "Optical low coherence method for characterizing silica-based arrayed-waveguide grating multiplexers," *J. Lightwave Technol.*, vol. 14, pp. 1677–1689, 1996.

[11] ——, "Origin of channel crosstalk in 100 GHz-spaced silica-based arrayed-waveguide grating multiplexer," *Electron. Lett.*, vol. 31, pp. 1176–1177, 1995.

[12] H. Yamada, K. Okamoto, A. Kanako, and A. Sugita, "Dispersion resulting from phase and amplitude error in arrayed-waveguide grating multiplexer-demultiplexers," *Opt. Lett.*, vol. 25, pp. 569–571.

[13] M. Zirngibl, C. Dragone, and C. H. Joyner, "Demonstration of a 15×15 arrayed-waveguide multiplexer on InP," *IEEE Photon. Technol. Lett.*, vol. 4, pp. 1250–1253, 1992.

[14] M. Kohtoku, H. Sanjoh, S. Oku, Y. Kadota, Y. Yoshikuni, and Y. Shibata, "InP-based 64-channel arrayed waveguide gratingwith 50 GHz channel spacing and up to -20 dB crosstalk," *Electron. Lett.*, vol. 33, pp. 1786–1787, 1997.

[15] M. Kohtoku, H. Sanjoh, S. Oku, Y. Kadota, and Y. Yoshikuni, "Polarization-independent InP arrayed waveguide grating filter using deep ridge waveguide structure," in *Proc. Lasers and Electro-Optics, 1997 CLEO/Pacific Rim'97*, pp. 284–285.

[16] Y. Hida, Y. Inoue, and S. Imamura, "Polymetric arrayed-waveguide grating multiplexer operating around 1.3 μm," *Electron. Lett.*, vol. 30, pp. 959–960, 1994.

[17] H. Okayama, M. Kawahara, and T. Kamijoh, "Reflective waveguide array multiplexer in LiNbO3," *J. Lightwave Technol.*, vol. 14, pp. 985–990, 1996.

[18] M. R. Amersfoort, C. R. de Boer, Y. S. Oei, B. H. Verbeek, P. Demeester, A. Looyen, and J. J. G. M. van der Tol, "Low-loss phased-array based 4-channel wavelength demultiplexer integrated with photodetectors," *IEEE Photon. Technol. Lett.*, vol. 6, pp. 62–64, 1994.

[19] M. Kohtoku, S. Oku, Y. Kadota, Y. Shibata, J. Kikuchi, and Y. Yoshikuni, "Unequally spaced 16 channel semiconductor AWG WDM monitor module with low crosstalk (<-24 dB) characteristics," in *ECIO'99*, 1999, Paper ThA2.

[20] M. Zirngibl, C. H. Joyner, and B. Glance, "Digitally tunable channel dropping filter/equalizer based on waveguide grating router and optical amplifier integration," *IEEE Photon. Technol. Lett.*, vol. 6, pp. 513–515, 1994.

[21] M. Zirngibl, C. Dragone, and C. H. Joyner, "Demonstration of a 15×15 arrayed-waveguide multiplexer on InP," *IEEE Photon. Technol. Lett.*, vol. 6, pp. 513–515, 1994.

[22] H. Ishii, M. Kohtoku, Y. Shibata, S. Oku, Y. Kadota, and Y. Yoshikuni, "Zero insertion loss operations in monolithically integrated WDM channel selectors," *IEEE Photon. Technol. Lett.*, vol. 11, pp. 242–244, 1999.

[23] E. Brinkmeyer and R. Ulrich, "High-resolution OCDR in dispersive waveguides," *Electron. Lett.*, vol. 26, pp. 413–414, 1990.

[24] A. Kohlhaas, C. Fromchen, and E. Brinkmeyer, "High-resolution OCDR for testing integrated-optical waveguide: Dispersion-corrupted experimental data corrected by a numerical algorithm," *J. Lightwave Technol.*, vol. 9, pp. 1493–1502, 1991.

[25] P.-L. Francois, M. Monerie, C. Vassallo, Y. Durteste, and F. R. Alard, "Three ways to implement interferencial techniques application to measurements of chromatic dispersion, birefringence, and nonlinear susceptibilities," *J. Lightwave Technol.*, vol. 7, pp. 500–513, 1988.

[26] R. K. Hickernell, K. Takada, M. Yamada, M. Shimizu, and M. Horiguchi, "Pump-induced dispersion of erbium-doped fiber measured by Fourier-transform spectroscopy," *Opt. Lett.*, vol. 18, pp. 19–20, 1993.

[27] J. Gehler and K. Losch, "Dispersion measurement of arrayed waveguide gratings by Fourier-transform spectroscopy," in *Proc. ECOC'99*, Nice, France, 1999, Paper I-368-369.

Hiroaki Yamada (M'00) was born in Shiga, Japan, on January 7, 1966. He received B.S. and M.S. degrees in electronics engineering from University of Osaka Prefecture, Osaka, Japan, in 1988 and 1990, respectively.

In 1990, he joined the NTT Laboratories, Ibaraki, Japan, where he has been engaged in research on silica-based planar lightwave circuits including arrayed-waveguide grating multi/demultiplexers and phase-trimming techniques.

Mr. Yamada is a member of the Institute of Electronics, Information and Communication Engineers (IEICE) of Japan and the Japan Society of Applied Physics.

Hiroaki Sanjoh was born in Hokkaido, Japan, in 1968. He received the B.E. and M.E. degrees in applied physics from Hokkaido University, Hokkaido, Japan, in 1990 and 1992, respectively.

In 1992, he joined the NTT Optoelectronics Laboratories, and engaged in research and development of semiconductor light sources for optical fiber communication systems. From 1998 to 2000, he engaged in research on photonic packet switching systems.

Masaki Kohtoku was born in Kochi Prefecture, Japan, on March 16, 1966. He received the B.E. and M.E. degrees in the Tokyo Institute of Technology, Department of Physical Electronics, Tokyo, Japan, in 1989 and 1991, respectively.

In 1991, he joined the NTT Photonics Laboratories, Kanagawa, Japan, where he was carrying out research on semiconductor waveguide devices.

Mr. Kohtoku is a member of the Institute of Electronics, Information, and Communication Engineers (IEICE) of Japan and the Japan Society of Applied Physics.

Kazumasa Takada (M'96) was born in Saitama Prefecture, Japan, on May 14, 1955. He received B.S. degree in physics from Saitama University, Japan, in 1979, and the M.S. degree in physics and the Ph.D. degrees in electronics engineering from the University of Tokyo, Japan, in 1981, 1993, respectively.

In 1981, he joined NTT Electrical Communication Laboratories, Japan, where he worked on research on birefringent polarization-maintaining fibers and optical fiber gyroscopes. From 1989 to 1992, he was involved in research on photonic switching systems. Since 1992, he has been involved in research on high-resolution reflectometry for planar lightwave circuits.

Dr. Takada is a member of the Institute of Electronics, Information and Communication Engineers (IEICE) of Japan and the Japan Society of Applied Physics.

Katsunari Okamoto (M'85–SM'98) was born in Hiroshima, Japan, on October 19, 1949. He received B.S., M.S., and Ph.D. degrees in electronics engineering from the University of Tokyo, Tokyo, Japan, in 1972, 1974, and 1977, respectively.

He joined Ibaraki Electrical Communication Laboratory, Nippon Telegraph and Telephone Corporation, Ibaraki, Japan, in 1977, and was engaged in the research on transmission characteristics of multimode, dispersion-flattened single-mode, single-polarization (PANDA) fibers, and fiber-optic components. He proposed for the first time the dispersion-flattened fiber (DFF) and succeeded in fabrication of DFF that had chromatic dispersion less than $\pm$1ps/km/nm over a wide spectral range. Since 1990, he has been working on the analysis and the synthesis of guided-wave devices, the computer-aided design and fabrication of silica-based planar lightwave circuits (PLCs) at Ibaraki R&D center, NTT Photonics Laboratories. He has developed a 256 $\times$ 256 star coupler, various kind of AWGs ranging from 8 ch to 50 nm spacing AWGs to 128 ch-25 GHz AWGs, flat spectral response AWGs and integrated-optic reconfigurable add/drop multiplexers. He is currently a head of Okamoto Research Laboratory. His group aims at development of highly functional waveguide devices for the next generation photonic networks. He has published more than 160 papers in technical journals and international conferences. He authored and coauthored eight books.

Dr. Okamoto is a member of the Optical Society of America (OSA), the Institute of Electronics, Information and Communication Engineers (IEICE) of Japan, and the Japan Society of Applied Physics.